Geochemistry, Geophysics, Geosystems

RESEARCH ARTICLE
10.1029/2020GC009225

Special Section:
Tethyan dynamics: from rifting to collision

Paleomagnetism of the Middle Cenozoic Mula Basin (East Tibet): Evidence for km-Scale Crustal Blocks Rotated by Midlower Crust Drag

Alessandro Todrani[1,2], Bo Zhang[3], Fabio Speranza[2], and Siyu Chen[3]

[1]Department of Sciences, Roma Tre University, Rome, Italy, [2]Istituto Nazionale di Geofisica e Vulcanologia, Rome, Italy, [3]School of Earth and Space Science, Peking University, Beijing, China

Key Points:
- We report on the paleomagnetism of middle Cenozoic red beds from the Mula basin (East Tibet)
- The basin is fragmented in 2–5 km wide crustal blocks showing irregular rotation pattern
- We suggest that post-20 Ma SE-ward directed midlower crust flow drag and rotated randomly upper crust blocks

Correspondence to:
A. Todrani,
alessandro.todrani@uniroma3.it

Citation:
Todrani, A., Zhang, B., Speranza, F., & Chen, S. (2020). Paleomagnetism of the middle Cenozoic Mula Basin (East Tibet): Evidence for km-scale crustal blocks rotated by midlower crust drag. *Geochemistry, Geophysics, Geosystems*, *21*, e2020GC009225. https://doi.org/10.1029/2020GC009225

Received 4 JUN 2020
Accepted 13 AUG 2020
Accepted article online 18 AUG 2020

Abstract Existing models describing continental crust deformation require the coexistence of strike-slip faults and crustal blocks rotating between them, although the dimension and shape of the blocks and the location and offset of the faults are mostly unconstrained. Here we report on the paleomagnetism of middle Cenozoic (<45 Ma) continental red beds exposed along the 40 km long and 2–8 km wide NW-trending Mula basin (East Tibet), unconformably lying above Triassic marine strata and plutons and mildly deformed by two subparallel thrust faults. A tectonic magnetic fabric and magnetic lineations subhorizontal and parallel to the compressive fronts show that thrust tectonics guided basin formation and continued soon after sediment deposition. Characteristic and high-temperature components isolated at 17 sites support a positive fold test and suggest primary detrital magnetization acquisition. The comparison with East Asia paleopoles defines several 2–5 km wide crust fragments yielding variable rotations from ~30° counterclockwise to ~90° clockwise without clear rotation trend. No strike-slip fault with offset exceeding 1 km occurs among blocks, and no regional-scale strike-slip fault is documented at basin vicinity, implying that the East Tibet rotation pattern is different from all existing block rotation models. A regional high thermal flow and vigorous geothermal activity are consistent with the occurrence of a ductile crust layer identified by seismological data at 13–30 km depths. We suggest that midlower crust, flowing SE-ward toward Indochina, drag upper crust fragments that were randomly rotated depending on the local torque exerted on lower block boundaries by a ductile crust flow.

1. Introduction

The patterns and kinematics of continental crust deformation within high plateaus of Earth underlain by thick crust and zones of diffused crustal deformation, such as the Altiplano-Puna Plateau (central Andes), Anatolia-Armenia-Iran, and Tibet, have long been a matter of debate (e.g., Dayem et al., 2009; François et al., 2014; Houseman & England, 1993; Lamb & Hoke, 1997; Molnar et al., 1973; Royden et al., 1997, 2008; Tapponnier et al., 1982, 2001). Current deformation is witnessed by GPS data that however have a maximum density of one station every tens to hundreds of square kilometers (in SE Tibet typically every 2,000–10,000 km^2; Gan et al., 2007; Figure 1a), thus can hardly document the style of crust deformation at a smaller kilometer-size scale. Moreover, GPS data can be influenced by transient deformation of seismic cycles related to neighbor active faults that may hinder the finite deformation accumulated over geologic timescales (Moreno et al., 2011).

In the past, paleomagnetic data gathered over orogenic deformation zones were used to propose several models of crust deformation, where strike-slip faults and rotating crustal blocks of variable size and shape were inferred to interact according to different geometries and kinematics (Hernandez-Moreno et al., 2014, 2016, and references therein). Such models always require the occurrence of at least one master strike-slip fault guiding block rotation and/or crust fragmentation into crust slates in turn separated by second-order strike-slip faults.

However, such models were rarely based over solid evidence, as the paleomagnetic data were typically sparse (few data every tens of square kilometers), and some of the strike-slip faults (mostly the second-order faults) were in fact not apparent in the field. More recently, paleomagnetic results with a higher spatial density, that is, several sites per few square kilometer, were collected at several regions such as New Zealand, South Chile, and Indochina (Hernandez-Moreno et al., 2014; Li, Advokaat, et al., 2017; Li et al., 2018; Pellegrino

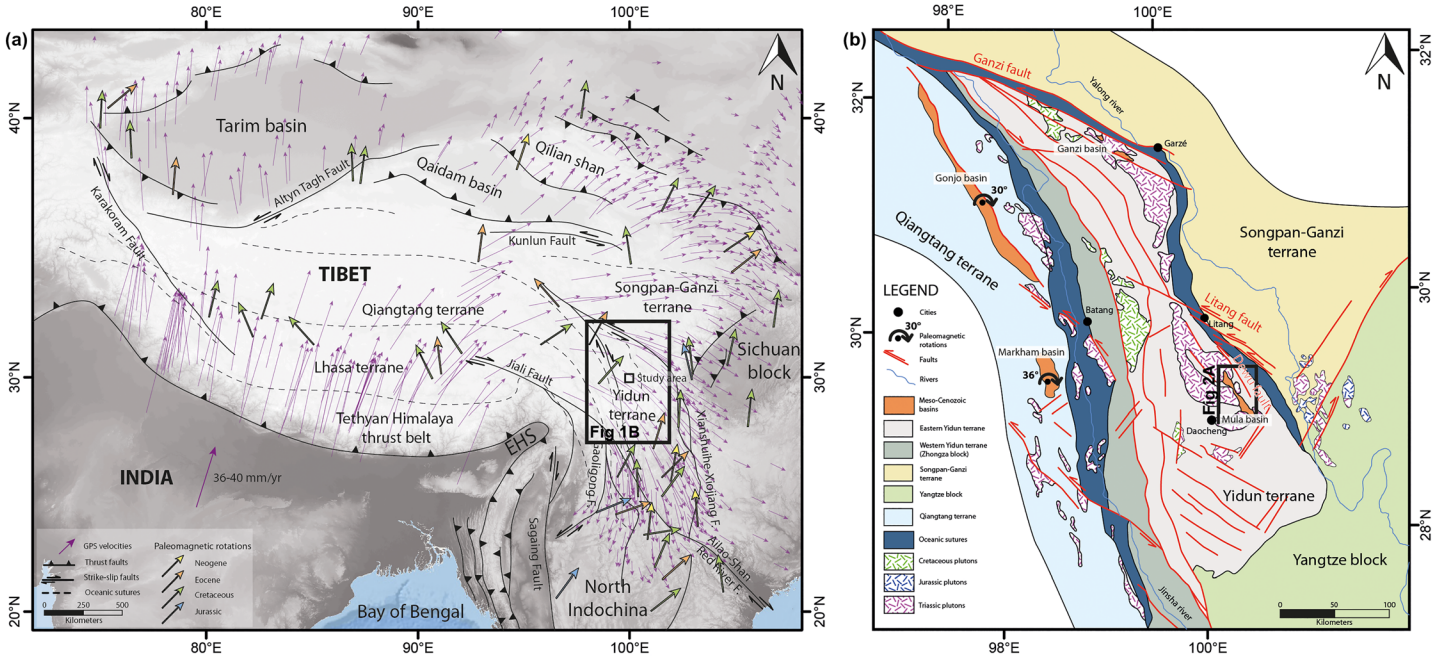

Figure 1. (a) Schematic tectonic map of the SE Asia generated by GIS (DEM source: Esri, User Community, geographic information system. Coordinate System & Projection: World Geodetic System 1984—Web Mercator Auxiliary Sphere). Purple thin arrows represent the present-day global positioning system velocities relative to stable Eurasia (Gan et al., 2007). Colored arrows are paleomagnetic rotations with respect to East-Asia poles by Cogné et al. (2013). Strike-slip fault shear senses are relative to Holocene times. EHS = East Himalaya Syntaxis. (b) Geological map of the Yidun terrane and previous paleomagnetic rotation data (Huang et al., 1992; Tong et al., 2017).

et al., 2018; Randall et al., 2011; Speranza et al., 2019). Such studies indeed recognized the occurrence of semirigidly crustal blocks and slates whose width varies between approximately 1 and 10 km that underwent independent paleomagnetic rotations. However, also in such cases, the great majority of the faults bounding rotating blocks was simply inferred. In fact, widespread occurrence of a fluvioglacial and volcanic blanket (Chile) or tropical vegetation developed above monotonous and easily erodible clayey-sandy red bed sequences (Indochina) commonly hides the geologic substratum.

Here we report on a paleomagnetic study of middle Cenozoic continental red beds exposed along the NW-elongated Mula basin, unconformably lying above deformed grayish-whitish Triassic marine strata and late Triassic plutons in the Yidun terrane of East Tibet. We puzzling document the occurrence of 2–5 km wide semirigid blocks undergoing independent rotations—both clockwise (CW) and counterclockwise (CCW) in sense—that are not separated by faults yielding significant displacements.

2. Geological Setting

The Yidun terrane is located in the E-SE Tibet, separated from the Qiangtang and the Songpan-Ganzi terranes by two Triassic ophiolitic mélange zones (Figure 1b). It is ~500 km long and ~160 km wide and mainly composed by 5 to 12 km thick Triassic turbidite and volcano-sedimentary sequences (Yidun Group rocks) and Late Triassic arc-related granitoid intrusions (Daocheng pluton), associated to the westward subduction of the Ganzi-Litang oceanic slab during middle-late Triassic (Gao et al., 2018; Reid et al., 2007; Wu et al., 2017). During early-middle Cenozoic shortening, several intracontinental sedimentary basins developed in East Tibet (Gonjo, Mula, and Ganzi basins; Jackson, Robinson, Weislogel, Jian, & McKay, 2018; Jackson, Robinson, Weislogel, Shang, & Jian, 2018; Studnicki-Gizbert et al., 2008; Tong et al., 2017; Zhang et al., 2018 Figure 1b).

The NW-oriented, ~40 km long, and 2–8 km wide Mula basin lies on top of the SE Yidun terrane (Figures 2 and 3) and is considered by Jackson, Robinson, Weislogel, Jian, and McKay (2018) as a flexural basin formed above a thrust fault footwall. It is filled by ~1 km thick oxidized, red to purple continental red beds deposited in alluvial environment, showing a maximum 45 ± 0.5 Ma (middle-lower Eocene) depositional age from

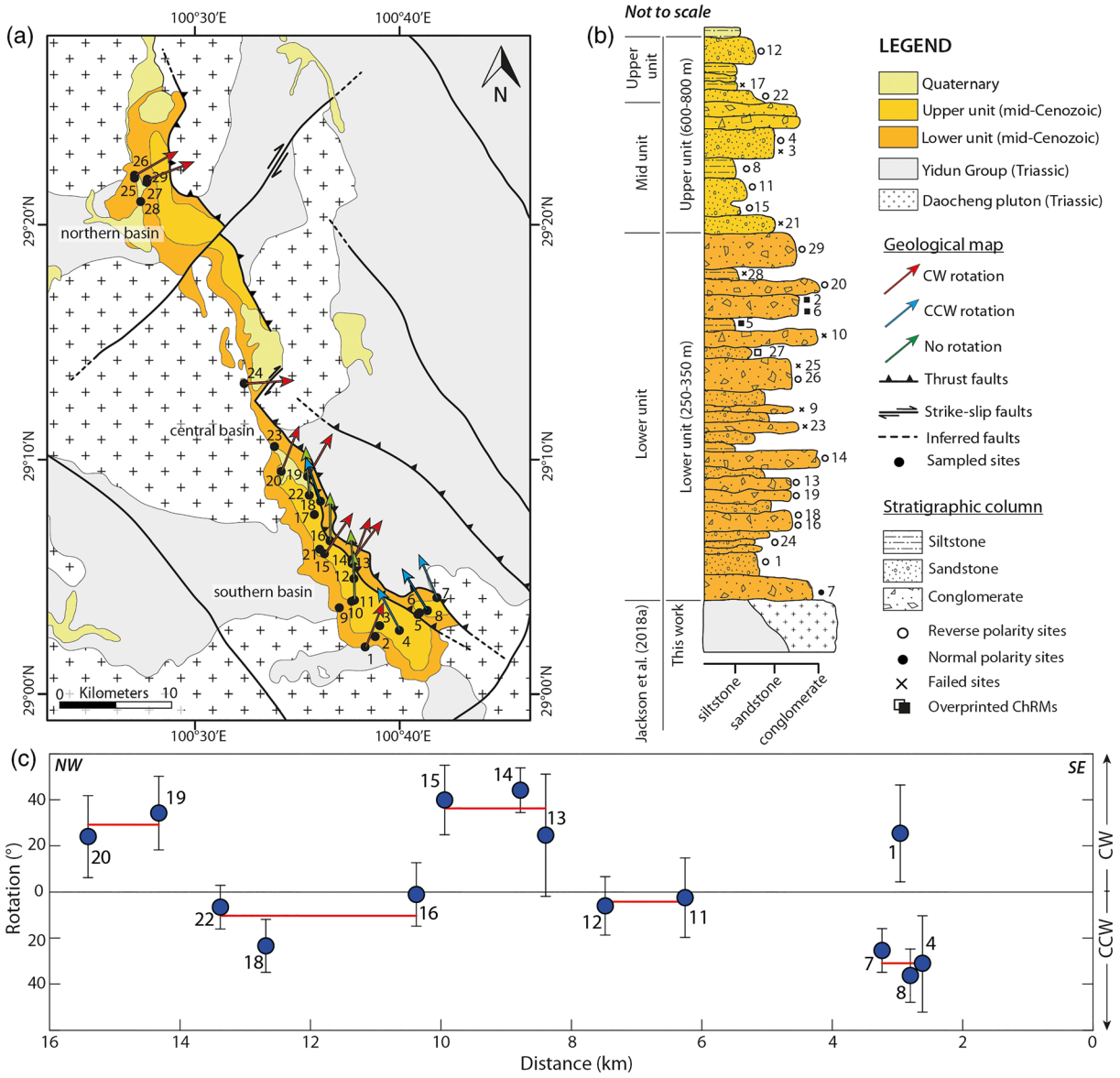

Figure 2. (a) Schematic geological map of the Mula basin and (b) stratigraphic column of the paleomagnetically sampled middle Cenozoic red beds. Black dots in (a) indicate the location of the 29 paleomagnetic sampled sites (MUL suffix is omitted). Colored arrows represent the CW (red), CCW (blue), and null (green) paleomagnetic rotations with respect to East-Asia. (c) Site-mean paleomagnetic rotations (and relative errors; Table 1) versus longitudinal distance (parallel to basin trend) in the southern Mula basin. Numbers refer to site numbers; the MUL suffix is omitted. Red lines represent the mean rotation values calculated from adjacent sites, defining individual 2–5 km wide blocks undergoing uniform rotation.

detrital zircon geochronology (Jackson, Robinson, Weislogel, Jian, & McKay, 2018). Along the SW basin margin, the Cenozoic continental strata unconformably overlay the Triassic Daocheng granites and the Yidun Group rocks. Conversely, the NE basin flank is characterized by a NE-dipping thrust fault juxtaposing the Triassic rocks on top of the red beds sequence (Bureau of Geology and Mineral Resources of Sichuan Province, 1984a, 1984b).

Jackson, Robinson, Weislogel, Jian, and McKay (2018) subdivided the Cenozoic deposits into three stratigraphic units, yet due to lithologic similarities, we consider here the two upper units altogether. The 350–400 m thick basal unit is characterized by 1–10 m thick reddish conglomerate beds interbedded to 0.1–1 m coarse-to-fine reddish-to-grayish sandstone layers (Figure 2b, 3a, and 3b). The conglomerate strata are made by matrix-supported layers hosting centimetric rounded to subangular clasts, alternated by thin centimetric layers of reddish-to-brown siltstone-mudstone. The 600–700 m thick upper unit (Figures 2b

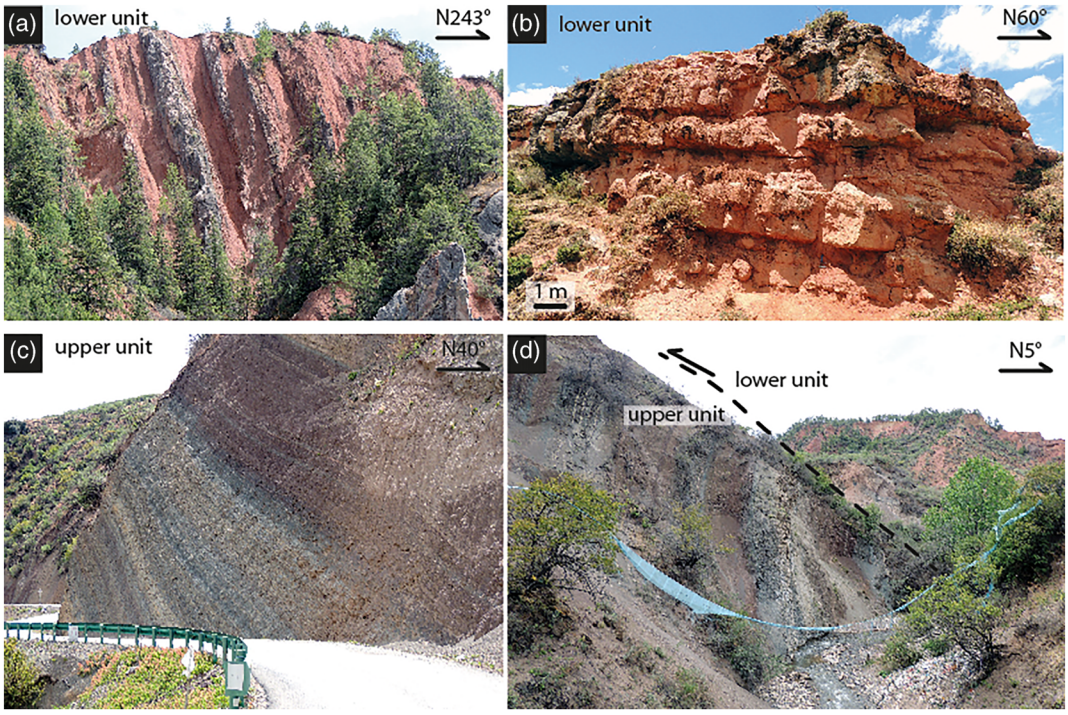

Figure 3. Field images of the lower (a, b) and upper (c, d) sedimentary units. Subvertical strata of Figure 2a are located just south of the boundary thrust fault (Site MUL08; Figure 2). (d) shows the intrabasin thrust fault juxtaposing the lower onto the upper unit.

and 3c) shows systematically reddish to purple fine sandstones interbedded with mudstone-to-siltstone levels. Matrix-supported sandstone strata are 0.1–1.5 m thick, intercalated to 5–30 cm thick massive mudstone and siltstone levels. Sporadic clast-supported conglomerate layers characterized by millimetric-to-centimetric subrounded clasts are also observed. Finally, thin virtually undeformed alluvial deposits generically referred to the Quaternary (Bureau of Geology and Mineral Resources of Sichuan Province, 1984a, 1984b) are observed on the top of the Cenozoic red beds.

In the southern Mula basin, a NE dipping thrust fault dissects the basin and juxtaposes the lower onto the upper unit (Figure 3d). The structural setting and stratigraphic features of the Cenozoic deposits that unconformably overlay the Triassic formations suggest a flexural development of the Mula basin due to incipient compressive tectonics, followed by similarly compressive postdepositional tectonics. Stratigraphic relationships show that the central northern basin and boundary thrust fault are cut by a NE-trending fault with dextral kinematics (Figure 2) that was not considered by Jackson, Robinson, Weislogel, Jian, and McKay (2018). Further south, the boundary thrust fault is dissected by a NE-trending tear fault showing an ~5 km dextral displacement. The study area is located at 15–40 km SW from some active NW-trending left-lateral strike-slip faults (Dewu and Litang faults; Wang & Burchfield, 2000; Zhang et al., 2015; Figure 1b).

More than 200 natural hot springs were mapped in the Yidun arc, consistently with a high measured geothermal heat flow (66 mW/m^2 on average; Tang et al., 2017). An unusual 13–30 km depth crust layer characterized by low seismic wave velocity and high Poisson's ratio is interpreted as related to hot and ductile middle crust (Moho is at ~ 60 km depth; Wang et al., 2019).

3. Paleomagnetic Sampling and Methods

A total number of 288 oriented samples from 29 sites was gathered in the Mula basin (Figure 2 and Table 1). At each site, we collected 8 to 11 (10 on average) paleomagnetic specimens, drilled using a portable drill cooled by water and oriented in situ using the Sun (when possible) and a magnetic compass, corrected for the local magnetic declination for the Year 2019 (1°W according to NOAA's Geophysical Data Center, https://www.ngdc.noaa.gov/geomag/declination.shtml). Sites were mostly sampled in the

Geochemistry, Geophysics, Geosystems

10.1029/2020GC009225

Table 1
Paleomagnetic Directions From the Mula Basin

Site	Geographic coordinates		Unit	Demagnetization component	Bedding (dip dir/dip)	*n*/*N*	In situ		Tilt corrected		*k*	α95 (deg)	*R* (deg)	Δ*R* (deg)	*F* (deg)	Δ*F* (deg)
	Latitude °N	Longitude °E					*D* (deg)	*I* (deg)	*D* (deg)	*I* (deg)						
MUL01	100.6389	29.0333	L	HT	14/30	6/10	210.1	−55.1	204.2	−25.8	12.6	19.7	21.2	17.5	12.3	16.1
MUL02[a]	100.6473	29.0407	L	ChRM	10/30	7/10	342.8	32.5	347.2	5.2	16.6	15.3	−15.7	12.5	32.9	12.8
MUL03	100.6509	29.0484	U	—	74/20	10/10	—	—	—	—	—	—	—	—	—	—
MUL04	100.6667	29.0450	U	ChRM	350/29	5/10	151.1	−49.6	156.9	−21.6	15.3	20.2	−26.0	17.4	16.4	16.4
MUL05[a]	100.6819	29.0564	L	ChRM	9/30	9/10	5.1	55.8	6.6	25.8	117.0	4.8	3.6	5.4	12.3	6.0
MUL06[a]	100.6831	29.0575	L	ChRM	33/42	9/10	7.4	49.4	16.4	9.9	42.4	8.0	13.5	7.2	28.2	7.8
MUL07	100.6974	29.0683	L	HT	228/119	9/10	330.6	−31.5	342.4	24.6	39.5	8.3	−21.2	7.9	13.5	8.0
MUL08	100.6897	29.0593	U	ChRM	242/108	9/10	182.5	10.0	152.7	−31.9	29.1	9.7	−30.2	9.6	6.2	8.9
MUL09	100.6179	29.0612	L	—	53/42	10/10	—	—	—	—	—	—	—	—	—	—
MUL10	100.6280	29.0657	L	—	43/21	10/10	—	—	—	—	—	—	—	—	—	—
MUL11	100.6302	29.0666	U	ChRM	62/21	6/10	161.8	−47.1	180.9	−40.0	25.1	13.6	−2.0	14.4	−1.9	11.6
MUL12	100.6299	29.0819	U	ChRM	37/19	8/10	166.0	−48.1	177.9	−34.5	29.0	10.5	−5.0	10.6	3.6	9.4
MUL13	100.6285	29.0926	L	HT	202/51	6/10	203.1	8.5	203.5	−42.5	12.0	20.2	20.5	22.1	−4.3	16.4
MUL14	100.6282	29.0954	L	HT	216/13	9/10	219.3	−23.6	219.8	−36.6	48.2	7.5	36.8	8.1	1.6	7.5
MUL15	100.6058	29.0996	U	HT	86/31	6/10	195.2	−45.1	216.2	−29.2	25.8	13.5	33.3	12.6	9.0	11.5
MUL16	100.6097	29.1081	L	HT	103/12	9/10	174.2	−32.5	182.1	−35.6	21.3	11.4	−0.9	11.5	2.6	10.0
MUL17	100.5977	29.1273	U	—	191/63	10/10	—	—	—	—	—	—	—	—	—	—
MUL18	100.6003	29.1348	L	HT	43/37	6/10	134.2	−43.5	163.5	−32.7	49.6	9.6	−19.5	9.6	5.5	8.8
MUL19	100.5922	29.1545	L	HT	80/55	4/10	172.1	−46.5	211.50	−23.3	38.2	15.1	28.6	13.3	14.9	12.7
MUL20	100.5707	29.1581	L	HT	105/20	4/10	192.1	−28.7	203.0	−27.8	33.0	16.2	20.0	14.8	10.4	13.5
MUL21	100.6021	29.1028	U	—	63/24	10/10	—	—	—	—	—	—	—	—	—	—
MUL22	100.5935	29.1410	U	HT	67/73	7/10	147.7	−23.5	177.5	−15.0	48.7	8.7	−5.5	7.9	23.2	8.2
MUL23	100.5654	29.1757	L	—	40/28	9/10	—	—	—	—	—	—	—	—	—	—
MUL24	100.5407	29.2204	L	HT	87/10	9/10	269.3	−34.5	269.1	−24.5	26.0	10.3	86.1	9.5	13.8	9.3
MUL25	100.4515	29.3663	L	—	72/26	10/10	—	—	—	—	—	—	—	—	—	—
MUL26	100.4514	29.3683	L	HT	81/31	5/10	234.8	−48.6	242.9	−19.7	24.6	15.7	60.0	13.5	18.8	13.1
MUL27[a]	100.4614	29.3633	L	HT	195/106	9/11	194.8	−38.8	15.2	−35.2	14.1	14.2	192.3	14.1	3.3	12.0
MUL28	100.4565	29.3496	L	—	275/3	10/10	—	—	—	—	—	—	—	—	—	—
MUL29	100.4619	29.3654	L	HT	138/14	8/10	249.3	−12.5	251.6	−7.1	84.4	6.1	68.6	6.0	31.4	6.6

Note. Unit: L = lower unit; U = upper unit. Demagnetization component: HT = high temperature (600–690°C); ChRM = characteristic remanent magnetization (300–690°C). Bedding is expressed in dip azimuth/dip values. *D* and *I* are site mean declination and inclination calculated before and after tectonic correction; *k* and α95 are statistical parameters after Fischer (1953); *n*/*N* is the number of samples giving reliable results/number of studied samples at a site. Site mean rotation *R* and flattening *F* values and relative errors Δ*R* and Δ*F* (according to Demarest, 1983) are relative to coeval *D* and *I* values expected at the sampling area considering East-Asia paleopoles from Cogné et al. (2013).
[a]Remagnetized sites.

lower reddish Mula basin unit (20 over 29 sites), spreading as much as possible each core on different stratigraphic levels, in order to average out the paleosecular variation of the geomagnetic field. We collected 11 sites (MUL01–11) in the southern basin sector (Figure 2a), sampling both the footwall and the hanging wall of the longitudinal intrabasin thrust fault. Twelve sites (MUL12–23) were sampled on both stratigraphical units in the central part of the Mula basin, and six sites (MUL24–29) were drilled in the lower unit from the northern sampling area.

Samples were cut into standard cylindrical specimens of 22 mm height, and paleomagnetic measurements were carried out in the shielded room of the paleomagnetic laboratory of the Istituto Nazionale di Geofisica e Vulcanologia (Rome, Italy), using a 2G Enterprises direct current superconducting quantum interface device cryogenic magnetometer. All samples were thermally demagnetized using a Pyrox shielded oven in 12 steps up to 690°C. Considering previous evidence from red beds paleomagnetically studied worldwide (Tanaka et al., 2008; Tong et al., 2017, among many others), the stepwise thermal demagnetization was performed using wide temperature increments (50°C) from 300°C to 600°C and smaller increments (15°C) between 600°C and 690°C, a temperature interval where the primary detrital magnetization component is generally isolated (Jiang et al., 2015). Demagnetization data were plotted on orthogonal diagrams (Zijderveld, 1967) and analyzed by principal-component analysis. Site-mean paleomagnetic directions were computed using Fischer (1953) statistic and plotted on equal-area projection. Rotation and flattening values with respect to Eurasia were evaluated according to Demarest (1983), using East-Asia paleopoles by Cogné et al. (2013). In order to analyze red bed magnetic fabric, the Anisotropy of Magnetic Susceptibility (AMS) at room temperature was performed for 272 specimens with an AGICO Kappabridge KLY-5 susceptibility bridge, and data were evaluated using Jelinek and Kropáček (1978) statistics.

Finally, one representative specimen from each site was selected for magnetic mineralogy analysis. A three-component isothermal remanent magnetization was first given to specimens by imparting 2.7, 0.6, and 0.12 T magnetic fields along the three sample axes with a 2G Enterprises pulse magnetizer and subsequently thermally demagnetized in 11 steps up to 680°C according to Lowrie (1990).

4. Results

4.1. Magnetic Mineralogy

The soft (<0.12 T) magnetic fraction is virtually absent, while the intermediate (0.12 < coercivity < 0.6 T) and high coercivity (0.6 < coercivity < 2.7 T) components are demagnetized at 680°C (Figure 4), pointing to hematite as the main magnetic carrier and confirming previous widespread evidence from SE Asia red beds (e.g., Speranza et al., 2019; Tong et al., 2017). A steep thermal decay at 120°C of the hard magnetic fraction is observed in 7 out of 29 samples from both sedimentary units, suggesting the occurrence of goethite along with hematite at few sites.

4.2. Paleomagnetic Directions and Rotations

Twenty-one out of 29 sites gave reliable paleomagnetic results, while the remaining eight sites were discarded from further consideration as they yielded scattered demagnetization diagrams. During the thermal demagnetization, a viscous component was isolated up to 300°C, and a characteristic remanent magnetization component (ChRM) was isolated in seven sites between 300°C and 690°C (Figures 5a, 5b, 5c, and 5e). In the remaining 14 sites, a low-temperature (LT) and high-temperature (HT) components were isolated in the 300–600°C and 600–690°C temperature intervals, respectively (Figures 5d, 5f, 5g, and 5h). Site-mean directions from LT magnetization component were obtained at eight sites (Figures 6a and 6b). The in situ LT components (excluding Site MUL24) are close to the present-day geocentric axial dipole (GAD) field direction expected for the sampling area ($D = 0°$, $I = 47°$; the fold test according to McFadden, 1990, is indeterminate), suggesting that they represent a recent chemical magnetic overprint, as frequently observed in red beds (Jiang et al., 2015; Li, Yang, et al., 2017; Liu et al., 2011).

Combining ChRMs and HT components, well-defined ($4.8° \leq \alpha_{95} \leq 20.2°$; 12.3° on average) site-mean directions were obtained for 21 paleomagnetic sites (Figures 6c and 6d and Table 1). Sites MUL02, MUL05, and MUL06—systematically defined by ChRMs from the southern Mula basin—showed again mean directions close to the present-day GAD field direction in in situ coordinates and anomalously low (5.2°, 25.8°, and 9.9°, respectively) inclinations in tilt-corrected coordinates (the 40 Ma East Asia expected inclination is 38° ± 6°),

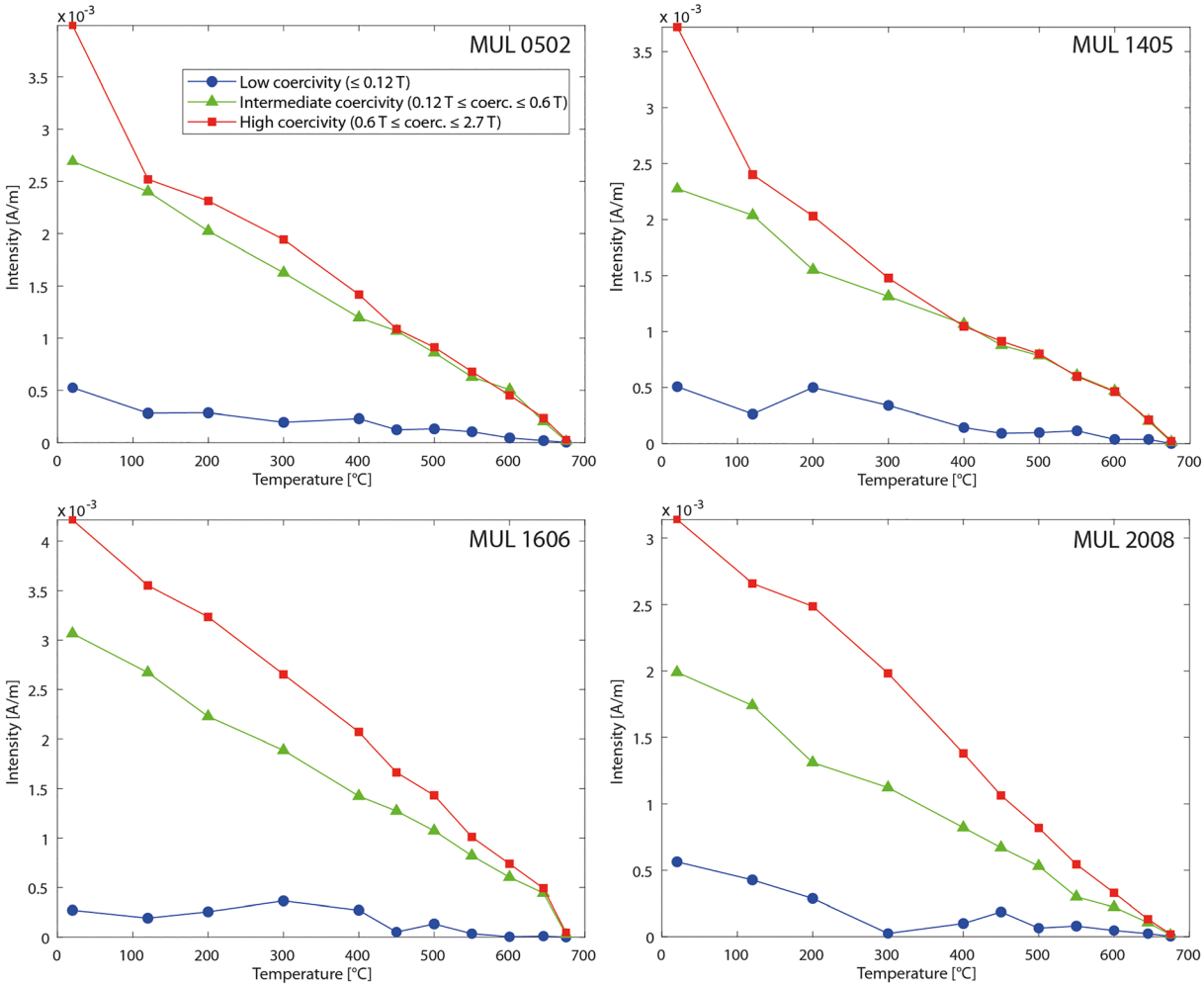

Figure 4. Thermal demagnetization of three-components IRM, according to Lowrie (1990), for four representative specimens from the Mula basin.

suggesting again a recent magnetic overprint. Furthermore, Site MUL27 from the northern Mula basin yielded an aberrant tilt-corrected direction completely different from that of neighbor sites and an in situ direction close to the local reverse-polarity GAD field; consequently, we assume that it was overprinted in a reverse-polarity chron. Thus, considering the—likely reliable—remaining 17 sites data set, a reverse magnetic polarity was systematically observed, except Site MUL07 from the lower sequence at the southern basin that yielded a normal polarity.

A systematic magnetic declination difference is observed in the southern and central-northern Mula basin sectors (Figures 2 and 6). Among the 17 reliable sites, three sites from the central-northern basin show westward directed declinations, whereas the other 14 sites from the southern sector yield SSE-ward to SSW-ward directed declinations (in the reverse-polarity state). The McFadden (1990) fold test applied on the 14 more clustered sites from the southern Mula basin supports a positive fold test at a 99% confidence level ($N = 14$; 99% critical Scos value = 6.08, $Scos_{instu} = 6.13$, $Scos_{tiltcorrected} = 3.12$; maximum K and minimum Scos values are obtained at 78% and 77% of complete unfolding, respectively). The McFadden and McElhinny (1990) reversal test applied on the 14 more clustered sites is undetermined.

The positive fold test, coupled with a folding age that is considered to occur just after (i.e., within few million years) sediment deposition, strongly suggests a primary late Eocene-early Oligocene (the preferred sediment age by Jackson, Robinson, Weislogel, Jian, & McKay, 2018) magnetization of the 17 reliable sites. The primary origin of the isolated ChRMs and HT components is also suggested by the convex shape of the NRM thermal decay curves and sudden remanence drop between 640°C and 690°C (Figure 5) that, according to

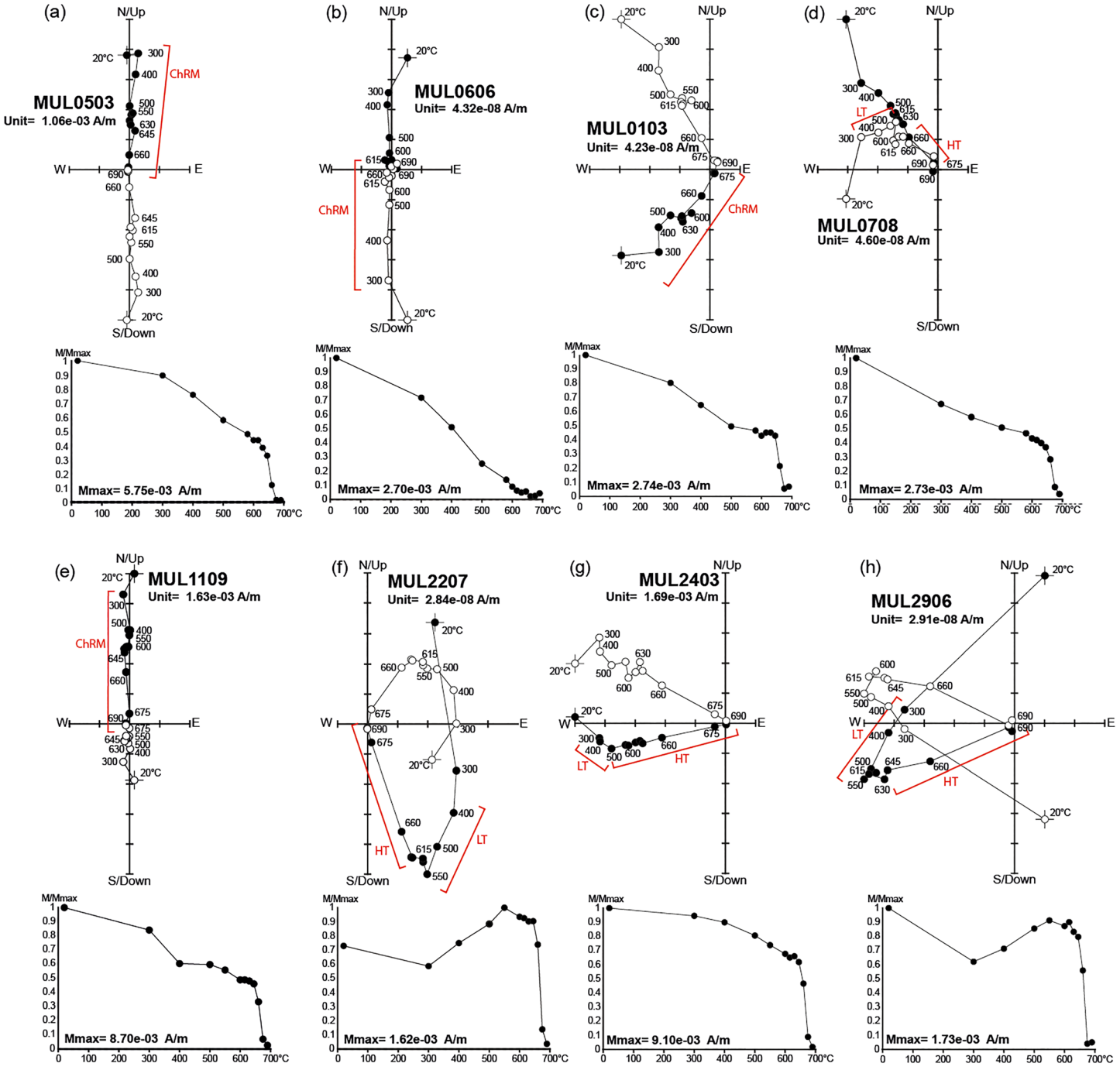

Figure 5. (a–h) Orthogonal vector diagram of representative demagnetization data, in situ coordinates. Progressive thermal demagnetization data are in °C. LT and HT are low-temperature and high-temperature magnetization components, respectively; ChRM is characteristics remanent magnetization component. Open and solid symbols represent projections on the vertical and horizontal planes, respectively.

Jiang et al. (2015), is typical for detrital hematite occurrence, whereas chemically overprinted hematite grains yield progressive demagnetization and concave decay curves.

Paleomagnetic rotations (Figures 2a–2c) calculated for the 17 reliable sites using the 40 Ma East-Asia paleomagnetic pole by Cogné et al. (2013) show several different rotational behaviors in the Mula basin. Three sites (MUL04-07-08) sampled at the SE basin edge show a systematic CCW rotation (average 26° ± 12°) with respect to East Asia. Eleven sites from the southern basin (MUL01 and from MUL10 to MUL23) show either null rotation or moderate (up to 37 ± 8°) CW rotations. Finally, the three sites from the northern Mula basin

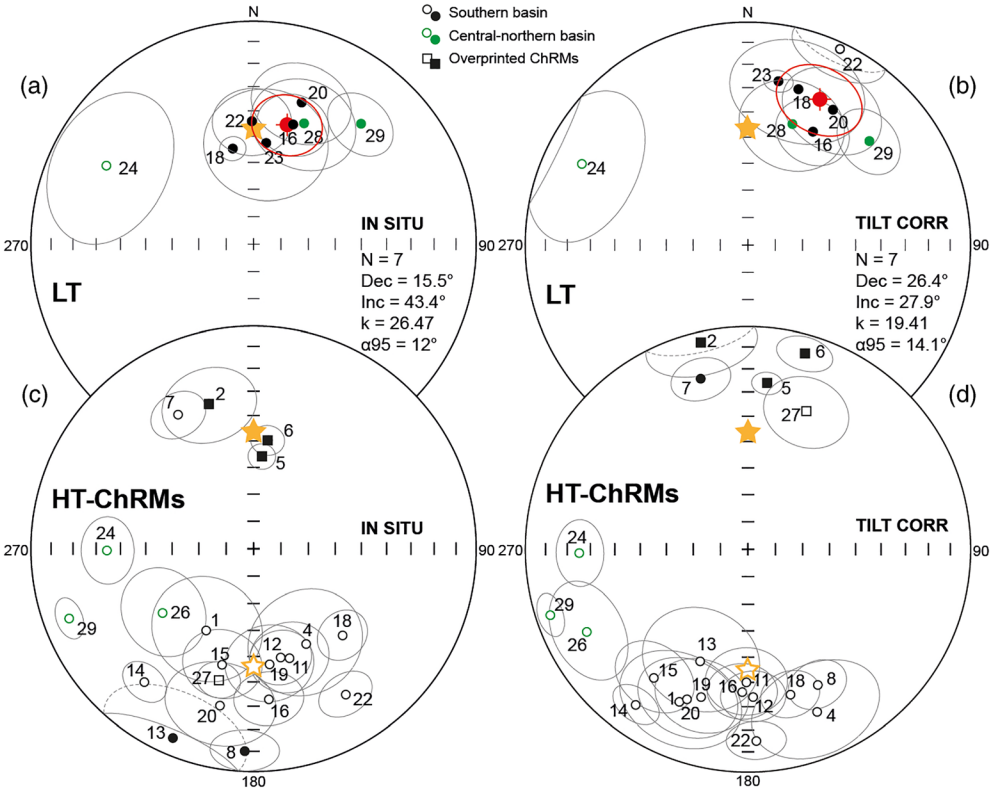

Figure 6. (a–d) Equal-area projection of the site-mean paleomagnetic directions, before (a, c) and after (b, d) tilt corrections. Solid (open) yellow star represents the normal (reverse) polarity geocentric axial dipole field direction ($D = 0°$, $I = 47°$ or $D = 180°$, $I = -47°$) expected for the study area. Solid (open) symbols represent projection onto the lower (upper) hemisphere, and open gray circles represent projections of the 95% confidence cones. Squares represent characteristics remanent magnetization components (ChRMs) that were inferred to be remagnetized. Red points and open circles represent the mean paleomagnetic directions of the low-temperature (LT) components and the relative 95% confidence cones, respectively. (upper panel) LT components isolated at eight sites (mean direction computed for seven sites, excluding Site MUL24). (lower panel) High-temperature components and ChRMs isolated at 21 sites.

show strong 60° to 86° CW rotations. Concerning inclination values, average flattening with respect to East Asia considering the 17 reliable sites (10.4° ± 11.1°; Table 1) is not significant.

4.3. AMS

Figure 7a shows the frequency distribution of the magnetic susceptibility values for the 272 specimens. The data set is characterized by mean susceptibility Km = (Kmax + Kint + Kmin)/3 clustered at low values, between 100 and 200 × 10–6 SI, suggesting a predominant contribution of paramagnetic clayey minerals to the magnetic susceptibility and fabric (e.g., Rochette et al., 1992). The parameters defining magnetic anisotropy (P′) and shape (T), according to Jelinek and Kropáček (1978), indicate moderate anisotropy (P′ < 1.09) and distributed fabrics, from oblate to prolate (Figures 7b and 7c).

The equal-area projection of the principal anisotropy axes shows a clustering of magnetic lineations (Kmax directions) along a subhorizontal N340° trend (Figures 7d–7g) which is subparallel to the orientation of both the Mula basin and the thrust faults bounding and cross-cutting it (Figure 2a). The magnetic foliations (planes orthogonal to Kmin directions) are mostly distributed at variable angles from bedding planes, with a main cluster that deviates by approximately 20° from bedding (Figure 7g).

5. Discussion

Magnetic lineations from the Mula basin are subhorizontal and mostly parallel to thrust fault trend, whereas magnetic foliation poles are distributed along a girdle pivoting around them. Such features clearly indicate a tectonic overprint of thrust tectonics on a sedimentary magnetic fabric (Weil & Yonkee, 2009, and references

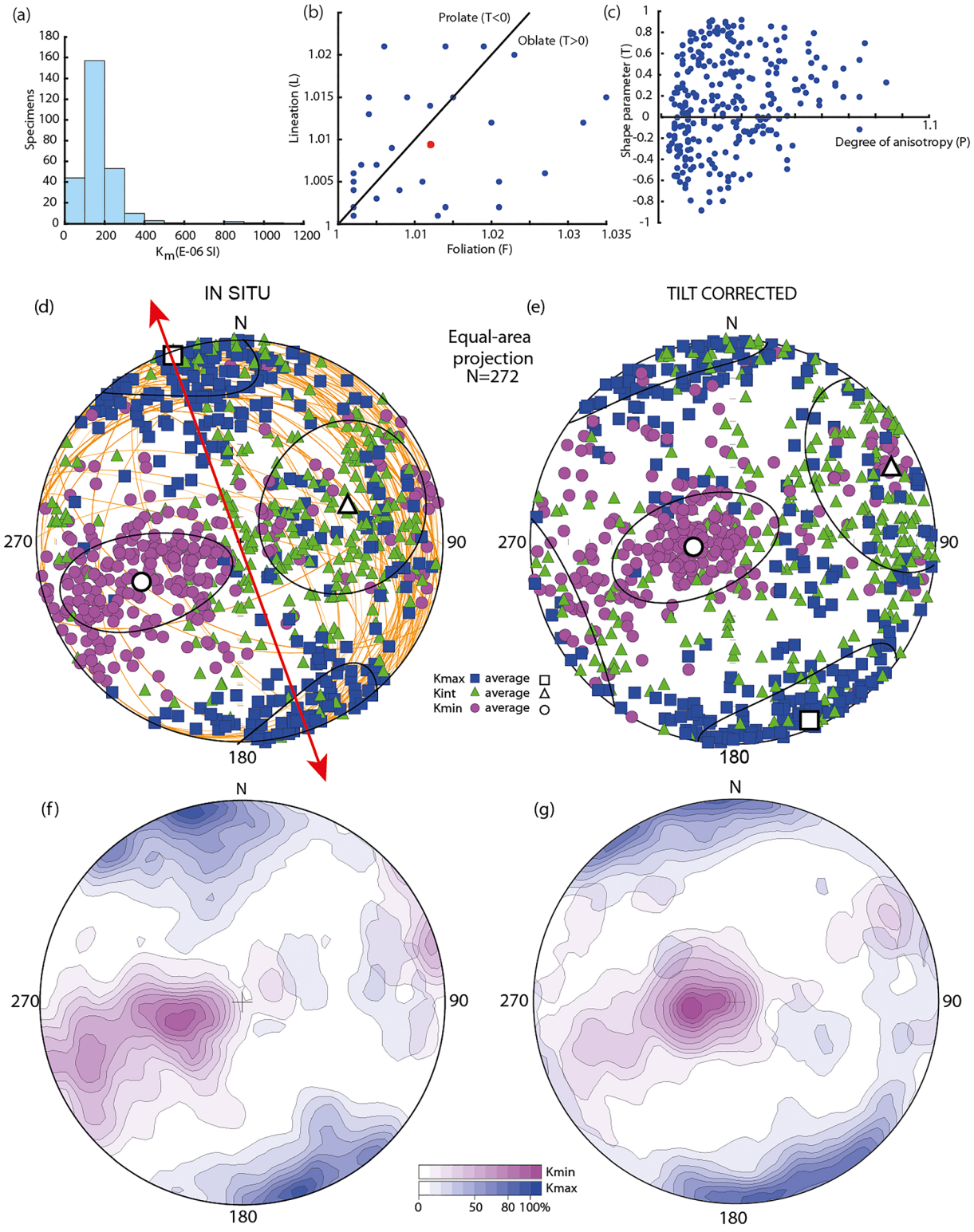

Figure 7. Anisotropy of Magnetic Susceptibility results from all investigated specimens ($N = 272$). (a) Frequency distribution of the mean susceptibility (km) values; (b) Flinn diagram: magnetic lineation (L) versus magnetic foliation (F) plot, the red dot represents the average value of the whole data set; (c) Jelinek diagram: anisotropy degree (P) versus shape parameter (T). Equal-area projection in situ (d) and tilt-corrected (e) coordinates of main anisotropy axes. The Kmax, Kint, and Kmin average values are reported in white with black ellipses; red arrow represents the mean Kmax orientation (magnetic lineation), and the orange semicircles represent projections of the bedding planes. (f, g) Contour plots of (d) and (e), respectively, represent the distribution of percentage densities of Kmax (blue) and Kmin (purple) axes.

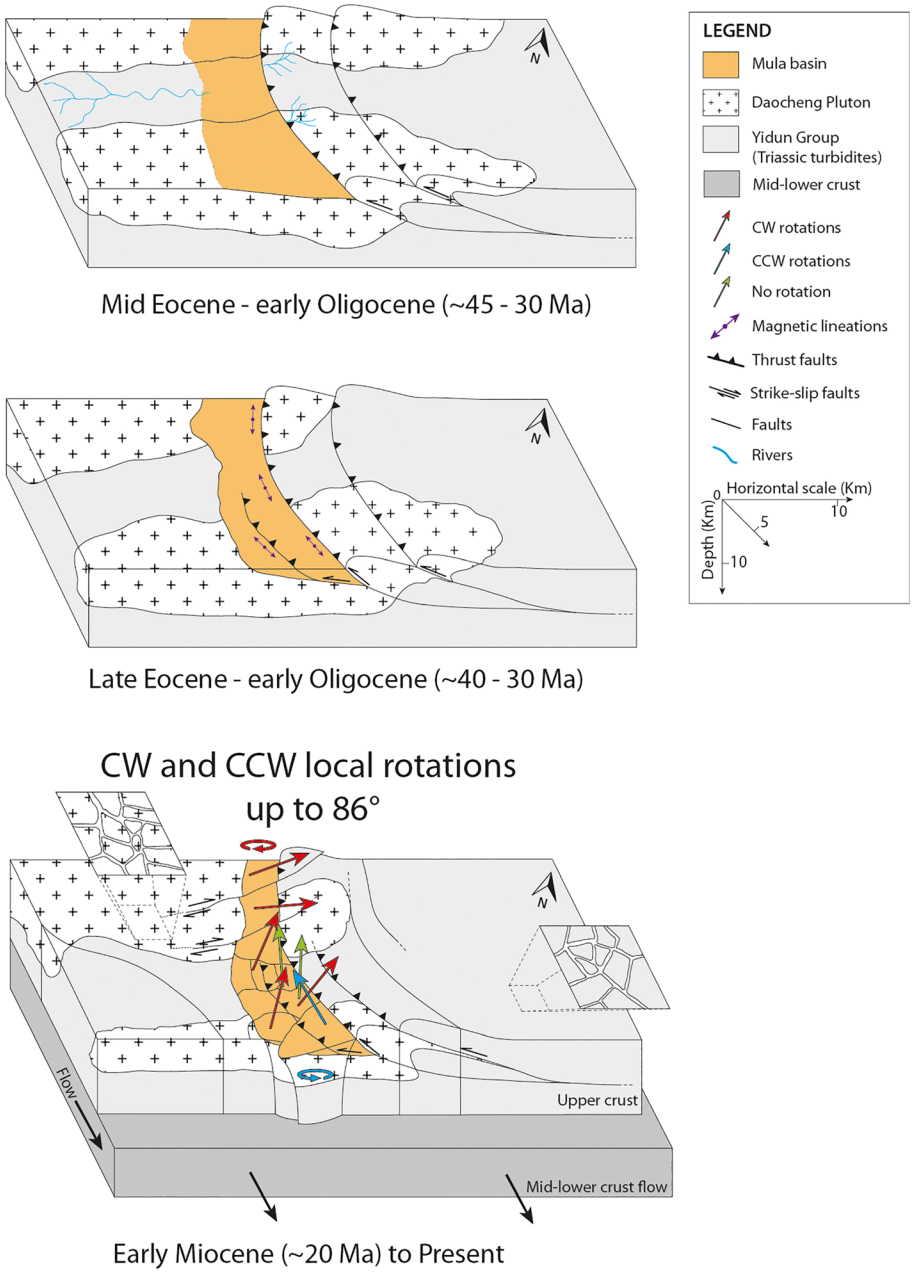

Figure 8. Three-stage crustal-scale evolution model of the formation and evolution of the Mula basin. Black thin arrows represent the magnetic lineation orientations. Paleomagnetic blocks rotation is reported with colored arrows: Red, blue, and green indicate CW, CCW, and no rotation, respectively.

therein). Several works documented that magnetic fabric of sediments is particularly sensitive to the pristine tectonic episodes occurring synchronous or just after sediment deposition (Mattei et al., 1997; Sagnotti et al., 1998). Thus, AMS data confirm that the Mula basin developed as a flexural basin adjacent to a NW-trending thrust front and that the thrust faults cross-cutting it formed soon after basin formation, likely during the same tectonic episode (Figure 8). A magnetic fabric completely comparable to that found by us was recently documented in the upper Cretaceous-lower Cenozoic Gonjo basin, located some 300 km NW of the Mula basin (Figure 1b; Li, van Hinsbergen, Shen, et al., 2020), confirming that similar tectonics characterized in lower-middle Cenozoic times the whole East Tibet.

AMS evidence also serves to exclude that the simple bed back-tilting we performed yields biased paleomagnetic data. In fact, in case of polyphase deformation or plunging structures, a simple bed back-tilting

translates into a wrong paleomagnetic direction, a classical problem for strongly deformed paleomagnetically sampled zones (MacDonald, 1980). Many studies showed in the past that in compressive settings, magnetic lineations from subparallel to local fold axes, meaning that in case of polyphase deformation and/or plunging folds, magnetic lineations are definitely not subhorizontal. Magnetic lineation is definitely a powerful proxy to get local fold axes directions that cannot be estimated by other methods (when folds are not apparent in the field, of course).

AMS data from the Mula basin show that magnetic lineations are mostly subhorizontal and subparallel to the thrust fronts (Figures 7d–7f), thus excluding the occurrence of plunging structures that would translate into biased paleomagnetic directions. This is also confirmed at southern basin edge by drag folds occurring in the red beds below the two thrust fronts that show subhorizontal axes.

Paleomagnetic data from the Mula basin reveal the occurrence of differently rotated blocks. Besides the three CCW rotated sites at SE basin edge, sites from the southern basin indicate the occurrence of small crustal blocks (2–5 km wide) alternating CW and null rotations (Figures 2a and 2c). Conversely, sites collected in the central-northern part of the basin show strong (60° to 86°) CW rotations, confirming block rotation occurrence although data resolution is not enough here to define block size. Only two NE-oriented faults of dextral kinematics offsetting the peripheral thrust fault of 1–2 km were mapped in the central-northern Mula basin (Figure 2a); however, they are far from almost all paleomagnetic sites, so that their effect on rotation pattern is unclear. Also, the rotations are not related to local effects of thrust fault(s) cutting the basin, as similar rotations occur at both basin sides, both adjacent and some kilometer away from thrust front(s) (see Sites MUL07-04, 19-20, and 29-26). Depending on crustal block size, paleomagnetic rotation magnitude, and other tectonic and geophysical parameters (e.g., crustal rheology, tectonic offset, and width of the fault zone), different crustal kinematics models were proposed during the last decades to justify the rotation pattern observed in transcurrent fault zones (Hernandez-Moreno et al., 2014, and references therein). Three main kinematics models were proposed, as they consider upper crust deformation as continuous (Kimura et al., 2011; McKenzie & Jackson, 1986), discontinuous (Ron et al., 1984), or quasi-continuous (Beck, 1976; Hernandez-Moreno et al., 2014; Randall et al., 2011; Sonder et al., 1994).

The continuous model considers paleomagnetic rotations systematically of the same sign continuously increasing toward the strike-slip fault, where they reach about 90° in magnitude; such rotation pattern is clearly not compatible with that from the Mula basin. The discontinuous model suggests a bookshelf (or domino) fault-slate system where elongated crust slates separated by strike-slip faults undergo rigid rotations. This model again is not verified in the Mula basin, as strike-slip faults separating rotating blocks in the southern basin are lacking (continuity of basin margins does not admit unrecognized faults with offsets greater than approximately 1 km; Figure 2a). Finally, the quasi-continuous model assumes that the rotation of the same sign of small crustal blocks increases getting closer to a master strike-slip fault, reaching values even largely exceeding 90° adjacent to the fault itself. Such model postulates that a thin viscous sheet in the midlower crust drags the brittle upper crust causing its fragmentation and block rotation. Again, such model is not consistent with the Mula basin setting, as a major strike-slip fault is lacking, and rotations vary irregularly from CCW to CW across the basin.

Early Cretaceous to Eocene paleomagnetic data collected in SE Tibet, NW of the Mula basin, predominantly reveal CW rotations although data resolution is usually not enough to highlight kilometer-size rotating blocks (Huang et al., 1992; Tong et al., 2015, 2017; Zhang et al., 2018; Li, van Hinsbergen, Najman, et al., 2020; Figure 1). Further south, a wealth of paleomagnetic data from north Indochina red beds similarly documented a complex pattern, with prevailing CW rotations, but also CCW rotated or unrotated crust blocks at some places (Tanaka et al., 2008; Li, Advokaat, et al., 2017; Li et al., 2018). Here crust fragmentation and independent rotating blocks in the 1–10 km size were documented both adjacent to major strike-slip faults (Pellegrino et al., 2018) and in the middle of "blocks" that were previously considered to be rigid and undeformed (Speranza et al., 2019).

The predominant CW rotation pattern from East Tibet and North Indochina has been mostly related to hundreds of kilometer wide blocks escaping SE-ward around the East Himalaya Syntaxis (EHS) as squeezed by India-Eurasia collision (Funahara et al., 1993; Otofuji et al., 2010; Li, Yang, et al., 2017; Li et al., 2018; Figure 1). Such rotation model was inspired by Tapponnier et al.'s (1982) and subsequent works that invoked the Oligo-Miocene E-SE-ward lateral extrusion of semirigid "megablocks" or "microplates" bounded by

continental-scale strike-slip (or transform) faults with displacements of several hundreds of kilometers that would cross the whole SE Asia.

Others conversely considered SE-ward Tibet crust drift shown by GPS data as driven by a thin viscous layer of a 10–15 km thick partial molten midlower crust occurring below 10–13 km depth, which would drag the brittle upper crust (Clark & Royden, 2000; Huang et al., 2019; Royden et al., 1997, 2008). The occurrence of an anomalous hot viscous layer in the midlower crust of the East Tibetan Plateau is confirmed by Helium isotopes data, a vigorous hydrothermal activity, and a high (51 to 80 mW/m^2) heat flow (Tang et al., 2017). GPS data (Gan et al., 2007; Liang et al., 2013) show that at present, the SE-ward crust extrusion reminds a glacier-like CW flow of SE Tibet and north Indochina around the EHS (Panda et al., 2019; Figure 1).

Paleomagnetic data from the Mula basin reveal a pervasive deformation of the crust and irregular rotations of 2–5 km wide blocks, certainly at odds with the occurrence of rigid continental-scale megablocks. Magnetic anisotropy data confirm that sediment deposition occurred in a flexural basin related to thrust tectonics, strengthening the suggestion of an early-middle Cenozoic NE-SW shortening that yielded crust thickening and the formation of numerous narrow continental basins in central-eastern Tibet (Clark, 2012; Studnicki-Gizbert et al., 2008; Wang & Burchfield, 2000). Thickening of the acidic crust caused an increase of radiogenic heat production and the formation of a weak and partially molten midlower crust layer.

Since ~15–20 Ma, the upper crust of East Tibet underwent a SE-ward lateral drift around the EHS, drag by the underlying ductile layer flowing SE-ward between the rigid crust buttresses represented by the EHS and the Sichuan block (Royden et al., 2008). We suggest that paleomagnetic rotations documented in the Mula basin reflect the drag of midlower crustal flow on brittle rigid crust. Small 2–5 km wide blocks are consistent with a shallow crustal décollement, and the irregular rotation pattern (with both CW and CCW rotations) coupled with lack of significant strike-slip faults bounding them suggests that rotations are driven by the local torque exerted on lower block boundaries by underlying ductile crust flow. Deep crust ductile flow interacted with a rigid crust shell probably already broken in small fragments by older tectonics. Differently than quasi-continuous models where rotations are systematically of the same sign and would depend upon lower crust drag gradient moving away from the master strike-slip fault zone, we suggest that unsystematic block rotations at the Mula basin depend on local blocks interactions with the remarkably constant lower crust flow shown by GPS data in SE Tibet.

6. Conclusions

The relation between magnetic anisotropy and compressive structural features from the middle Cenozoic Mula basin confirms that sediments deposited due to flexural subsidence and SW-ward thrust propagation in East Tibet. The basin was later disrupted into 2–5 km wide blocks that rotated irregularly both CCW (up to 30° ± 10°) and CW (up to 86° ± 10°) with respect to East Asia. Surprisingly, no fault with offset exceeding approximately 1 km exists among rotating blocks, and no regional-scale strike-slip fault is documented at basin vicinity, implying that the paleomagnetic rotation pattern cannot be explained by any of the block rotation models postulated so far. The suggestion of hundreds of kilometer wide crustal blocks or microplates—squeezed by India-Eurasia convergence thus escaping SE-ward from Tibet to SE Asia and rotating rigidly—is also not supported by our paleomagnetic data.

Late Cretaceous-middle Cenozoic shortening in Tibet caused radiogenic crust thickening and subsequent heating that eventually led to the formation of a layer of ductile and partially molten midlower crust (Huang et al., 2019). In early Miocene times (15–20 Ma), the ductile crust underwent lateral instability and started to flow SE-ward in a glacier-like manner toward Indochina, in between the rigid crust buttresses represented by the EHS and Sichuan block. We speculate that the constant lower crust flow documented in East Tibet drag and rotated randomly kilometer-size upper crust blocks, according to the local interaction between lower block geometry and underlying crust flow.

Data Availability Statement

All paleomagnetic data supporting this work are available at institutional INGV FTP site address (ftp://ftp.ingv.it/pub/alessandro.todrani/Data/).

Acknowledgments

Many thanks to Aldo Winkler for solving several problems in the lab. We are grateful to Shihu Li and an anonymous referee for providing constructive comments on the manuscript. Many thanks to the G-cubed Editors Joshua Feinberg and Claudio Faccenna for carefully handling of our work. A. T. gratefully acknowledges a Ph.D. grant from INGV and the Department of Sciences, Roma Tre University (MIUR-Italy Dipartimenti di Eccellenza, ARTICOLO 1, COMMI 314–337 LEGGE 232/2016).

References

Beck, M. E. (1976). Discordant paleomagnetic pole positions as evidence of regional shear in the western Cordillera of North America. *American Journal of Science*, *276*(6), 694–712. https://doi.org/10.2475/ajs.276.6.694

Bureau of Geology and Mineral Resources of Sichuan Province (1984a). Regional geology of Sichuan Province. Geological map H-47-XXIII, 1:200,000 scale, 1954 Beijing Coordinate System. In *Chinese*. Beijing: Geological Publishing House.

Bureau of Geology and Mineral Resources of Sichuan Province (1984b). Regional geology of Sichuan Province. Geological map H-47-XXIV, 1:200,000 scale, 1954 Beijing Coordinate System. In *Chinese*. Beijing: Geological Publishing House.

Clark, M. K. (2012). Continental collision slowing due to viscous mantle lithosphere rather than topography. *Nature*, *483*(7387), 74–77. https://doi.org/10.1038/nature10848

Clark, M. K., & Royden, L. H. (2000). Topographic ooze: Building the eastern margin of Tibet by lower crustal flow. *Geology*, *28*(8), 703–706. https://doi.org/10.1130/0091-7613(2000)28%3C703:TOBTEM%3E2.0.CO;2

Cogné, J. P., Besse, J., Chen, Y., & Hankard, F. (2013). A new Late Cretaceous to Present APWP for Asia and its implications for paleomagnetic shallow inclinations in Central Asia and Cenozoic Eurasian plate deformation. *Geophysical Journal International*, *192*(3), 1000–1024. https://doi.org/10.1093/gji/ggs104

Dayem, K. E., Molnar, P., Clark, M. K., & Houseman, G. A. (2009). Far-field lithospheric deformation in Tibet during continental collision. *Tectonics*, *28*, TC6005. https://doi.org/10.1029/2008TC002344

Demarest, H. (1983). Error analysis for the determination of tectonic rotation from paleomagnetic data. *Journal of Geophysical Research*, *88*(B5), 4321–4328. https://doi.org/10.1029/JB088iB05p04321

Fischer, R. A. (1953). Dispersion on a sphere. *Proceedings of the Royal Society of London, Series A*, *217*(1130), 295–305. https://doi.org/10.1098/rspa.1953.0064

François, T., Burov, E., Agard, P., & Meyer, B. (2014). Buildup of a dynamically supported orogenic plateau: Numerical modelling of the Zagros/Central Iran case study. *Geochemistry, Geophysics, Geosystems*, *15*, 2632–2654. https://doi.org/10.1002/2013GC005223

Funahara, S., Nishiwaki, N., Murata, F., Otofuji, Y., & Wang, Y. Z. (1993). Clockwise rotation of the Red River fault inferred from paleomagnetic study of Cretaceous rocks in the Shan-Thai-Malay Block of western Yunnan, China. *Earth and Planetary Science Letters*, *117*(1–2), 29–42. https://doi.org/10.1016/0012-821X(93)90115-P

Gan, W., Zhang, P., Shen, Z.-K., Niu, Z., Wang, M., Wan, Y., et al. (2007). Present-day crustal motion within the Tibetan plateau inferred from GPS measurements. *Journal of Geophysical Research*, *112*, B08416. https://doi.org/10.1029/2005JB004120

Gao, X., Yang, L.-Q., & Orovan, E. A. (2018). The lithospheric architecture of two subterranes in the eastern Yidun Terrane, East Tethys: Insights from Hf-Nd isotopic mapping. *Gondwana Research*, *62*, 127–143. https://doi.org/10.1016/j.gr.2018.02.010

Hernandez-Moreno, C., Speranza, F., & Di Chiara, A. (2014). Understanding kinematics of intra-arc transcurrent deformation: Paleomagnetic evidence from the Liquiñe-Ofqui fault zone (Chile, 38–41°S). *Tectonics*, *33*, 1964–1988. https://doi.org/10.1002/2014TC003622

Hernandez-Moreno, C., Speranza, F., & Di Chiara, A. (2016). Paleomagnetic rotation pattern of the southern Chile fore-arc sliver (38°S–42°S): A new tool to evaluate plate locking along subduction zones. *Journal of Geophysical Research: Solid Earth*, *121*, 469–490. https://doi.org/10.1002/2015JB012382

Houseman, G., & England, P. (1993). Crustal thickening versus lateral expulsion in the Indian-Asian continental collision. *Journal of Geophysical Research*, *98*(B7), 12,233–12,249. https://doi.org/10.1029/93JB00443

Huang, K., Opdyke, N. D., Li, J., & Peng, Z. (1992). Paleomagnetism of Cretaceous rocks from eastern Qiangtang terrane of Tibet. *Journal of Geophysical Research*, *97*, 1789–1799. https://doi.org/10.1029/91JB02747

Huang, Z., Wang, L., Xu, M., Zhao, D., Mi, N., & Yu, D. (2019). P and S wave tomography beneath the SE Tibetan Plateau: Evidence for lithospheric delamination. *Journal of Geophysical Research: Solid Earth*, *124*, 10,292–10,308. https://doi.org/10.1029/2019JB017430

Jackson, W. T. Jr., Robinson, D. M., Weislogel, A. L., Jian, X., & McKay, M. P. (2018). Cenozoic development of the nonmarine Mula basin in the Southern Yidun terrane: Deposition and deformation in the eastern Tibetan Plateau associated with the India-Asia collision. *Tectonics*, *37*, 2446–2465. https://doi.org/10.1029/2018TC004994

Jackson, W. T. Jr., Robinson, D. M., Weislogel, A. L., Shang, F., & Jian, X. (2018). Mesozoic development of nonmarine basins in the northern Yidun terrane: Deposition and deformation in the eastern Tibetan Plateau prior to the India-Asia collision. *Tectonics*, *37*, 2466–2485. https://doi.org/10.1029/2018TC004995

Jelinek, V., & Kropáček, V. (1978). Statistical processing of anisotropy of magnetic susceptibility measured on groups of specimens. *Studia Geophysica et Geodaetica*, *22*, 50–62. https://doi.org/10.1007/BF01613632

Jiang, Z., Liu, Q., Dekkers, M. J., Tauxe, L., Qin, H., Barrón, V., & Torrent, J. (2015). Acquisition of chemical magnetization during experimental ferrihydrite-hematite conversion in Earth-like magnetic field-implications for paleomagnetic studies of red beds. *Earth and Planetary Science Letters*, *428*, 1–10. https://doi.org/10.1016/j.epsl.2015.07.024

Kimura, H., Ishikawa, N., & Sato, H. (2011). Estimation of total lateral displacement including strike-slip offset broader drag deformation on an active fault: Tectonic geomorphic and paleomagnetic evidence on the Tanna fault zone in Central Japan. *Tectonophysics*, *501*, 87–97. https://doi.org/10.1016/j.tecto.2011.01.016

Lamb, S., & Hoke, L. (1997). Origin of the high plateau in the Central Andes, Bolivia, South America. *Tectonics*, *16*, 623–649. https://doi.org/10.1029/97TC00495

Li, S., Advokaat, E. L., van Hinsbergen, D. J. J., Koymans, M., Deng, C., & Zhu, R. (2017). Paleomagnetic constraints on the Mesozoic-Cenozoic paleolatitudinal and rotational history of Indochina and South China: Review and updated kinematic reconstruction. *Earth-Science Reviews*, *171*, 58–77. https://doi.org/10.1016/j.earscirev.2017.05.007

Li, S., Van Hinsbergen, D. J. J., Deng, C., Advokaat, E. L., & Zhu, R. (2018). Paleomagnetic constraints from the Baoshan area on the deformation of the Qiangtang-Sibumasu Terrane around the eastern Himalayan syntaxis. *Journal of Geophysical Research: Solid Earth*, *123*, 977–997. https://doi.org/10.1002/2017JB015112

Li, S., van Hinsbergen, D. J. J., Najman, Y., Liu-Zeng, J., Deng, C., & Zhu, R. (2020). Does pulsed Tibetan deformation correlate with Indian plate motion changes? *Earth and Planetary Science Letters*, *536*, 116144. https://doi.org/10.1016/j.epsl.2020.116144

Li, S., van Hinsbergen, D. J. J., Shen, Z., Najman, Y., Deng, C., & Zhu, R. (2020). Anisotropy of magnetic susceptibility (AMS) analysis of the Gonjo Basin as an independent constraint to date Tibetan shortening pulses. *Geophysical Research Letters*, *47*, e2020GL087531. https://doi.org/10.1029/2020GL087531

Li, S., Yang, Z., Deng, C., He, H., Qin, H., Sun, L., et al. (2017). Clockwise rotations recorded in red beds from the Jinggu Basin of northwestern Indochina. *Geological Society of America*, *129*, B31637.1–B31637.1122. https://doi.org/10.1130/B31637.1

Liang, S., Gan, W., Shen, C., Xiao, G., Liu, J., Chen, W., et al. (2013). Three-dimensional velocity field of present-day crustal motion of the Tibetan Plateau derived from GPS measurements. *Journal of Geophysical Research: Solid Earth*, *118*, 5722–5732. https://doi.org/10.1002/2013JB010503

Liu, C., Ge, K., Zhang, C., Liu, Q., Deng, C., & Zhu, R. (2011). Nature of remagnetization of Lower Triassic red beds in southwestern China. *Geophysical Journal International*, *187*(3), 1237–1249. https://doi.org/10.1111/j.1365-246X.2011.05196.x

Lowrie, W. (1990). Identification of ferromagnetic minerals in a rock by coercivity and unblocking temperature properties. *Geophysical Research Letters*, *17*, 159–162. https://doi.org/10.1029/GL017i002p00159

MacDonald, W. D. (1980). Net tectonics rotation, apparent tectonic rotation, and the structural tilt correction in paleomagnetic studies. *Journal of Geophysical Research*, *85*, 3659–3669. https://doi.org/10.1029/JB085iB07p03659

Mattei, M., Sagnotti, L., Faccenna, C., & Funiciello, R. (1997). Magnetic fabric of weakly deformed clay-rich sediments in the Italian peninsula: Relationship with compressional and extensional tectonics. *Tectonophysics*, *271*(1-2), 107–122. https://doi.org/10.1016/S0040-1951(96)00244-2

McFadden, P. L. (1990). A new fold test for paleomagnetic studies. *Geophysical Journal International*, *103*(1), 163–169. https://doi.org/10.1111/j.1365-246X.1990.tb01761.x

McFadden, P. L., & McElhinny, M. W. (1990). Classification of the reversal test in paleomagnetism. *Geophysical Journal International*, *103*(3), 725–729. https://doi.org/10.1111/j.1365-246X.1990.tb05683.x

McKenzie, D., & Jackson, J. (1986). A block model of distributed deformation by faulting. *Journal of Geological Society*, *143*(2), 349–353. https://doi.org/10.1144/gsjgs.143.2.0349

Molnar, P., Fitch, T. J., & Wu, F. T. (1973). Fault plane solutions of shallow earthquakes and contemporary tectonics in Asia. *Earth and Planetary Science Letters*, *19*(2), 101–112. https://doi.org/10.1016/0012-821X(73)90104-0

Moreno, M., Melnick, D., Rosenau, M., Bolte, J., Klotz, J., Echtler, H., et al. (2011). Heterogeneous plate locking in the South–Central Chile subduction zone: Building up the next great earthquake. *Earth and Planetary Science Letters*, *305*(3-4), 413–424. https://doi.org/10.1016/j.epsl.2011.03.025

Otofuji, Y., Yokoyama, M., Kitada, K., & Zaman, H. (2010). Paleomagnetic versus GPS determined tectonic rotation around eastern Himalayan Syntaxis in East Asia. *Journal of Asian Earth Sciences*, *37*(5–6), 438–451. https://doi.org/10.1016/j.jseaes.2009.11.003

Panda, D., Mondal, A., & Kundu, B. (2019). Eastward "glacier-like flow" of the Tibetan crust constrained from power-law rheology. *Journal of Asian Earth Sciences*, *177*, 129–133. https://doi.org/10.1016/j.jseaes.2019.03.021

Pellegrino, A. G., Zhang, B., Speranza, F., Maniscalco, R., Yin, C., Hernandez-Moreno, C., & Winkler, A. (2018). Tectonics and paleomagnetic rotation pattern of Yunnan (24°N–25°N, China): Gaoligong fault shear versus megablock drift. *Tectonics*, *37*(5), 1524–1551. https://doi.org/10.1029/2017TC004899

Randall, K., Lamb, S., & Mac Niocaill, C. (2011). Large tectonic rotations in a wide zone of Neogene distributed dextral shear, northeastern South Island, New Zealand. *Tectonophysics*, *509*(3-4), 165–180. https://doi.org/10.1016/j.tecto.2011.05.006

Reid, A., Wilson, C. J. L., Shun, L., Pearson, N., & Belousova, E. (2007). Mesozoic plutons of the Yidun arc, SW China: U/Pb geochronology and Hf isotopic signature. *Ore Geology Reviews*, *31*(1-4), 88–106. https://doi.org/10.1016/j.oregeorev.2004.11.003

Rochette, P., Jackson, M., & Aubourg, C. (1992). Rock magnetism and the interpretation of anisotropy of magnetic susceptibility. *Reviews of Geophysics*, *30*, 209–226. https://doi.org/10.1029/92RG00733

Ron, H., Freund, R., & Garfunkel, Z. (1984). Block rotation by strike-slip faulting: Structural and paleomagnetic evidence. *Journal of Geophysical Research*, *89*, 6256–6270. https://doi.org/10.1029/JB089iB07p06256

Royden, L. H., Burchfiel, B. C., King, R., Wang, E., Chen, Z., Shen, F., & Liu, Y. (1997). Surface deformation and lower crustal flow in Eastern Tibet. *Science*, *276*(5313), 788–790. https://doi.org/10.1126/science.276.5313.788

Royden, L. H., Burchfiel, B. C., & Van der Hilst, R. D. (2008). The geological evolution of the Tibetan Plateau. *Science*, *321*(5892), 1054–1058. https://doi.org/10.1126/science.1155371

Sagnotti, L., Speranza, F., Winkler, A., Mattei, M., & Funiciello, R. (1998). Magnetic fabric of clay sediments from the external northern Apennines (Italy). *Physics of the Earth and Planetary Interiors*, *105*, 73–93. https://doi.org/10.1016/S0031-9201(97)00071-X

Sonder, L. J., Jones, C. H., Salyards, S. L., & Murphy, K. M. (1994). Vertical axis rotations in the Las Vegas Valley Shear Zone, southern Nevada: Paleomagnetic constraints on kinematics and dynamics of block rotations. *Tectonics*, *13*(4), 769–788. https://doi.org/10.1029/94TC00352

Speranza, F., Pellegrino, A. G., Zhang, B., Maniscalco, R., Chen, S., & Hernandez-Moreno, C. (2019). Paleomagnetic evidence for 25–15 Ma crust fragmentation of north Indochina (23–26°N): Consequence of collision with Greater India NE corner? *Geochemistry, Geophysics, Geosystems*, *20*, 5425–5448. https://doi.org/10.1029/2019GC008308

Studnicki-Gizbert, C., Burchfiel, B. C., Li, Z., & Chen, Z. (2008). Early Tertiary Gonjo basin, eastern Tibet: Sedimentary and structural record of the early history of India-Asia collision. *Geosphere*, *4*(4), 713–735. https://doi.org/10.1130/GES00136.1

Tanaka, K., Mu, C., Sato, K., Takemoto, K., Miura, D., Liu, Y., et al. (2008). Tectonic deformation around the eastern Himalayan Syntaxis: Constraints from the Cretaceous palaeomagnetic data of the Shan-Thai Block. *Geophysical Journal International*, *175*, 713–728. https://doi.org/10.1111/j.1365-246X.2008.03885.x

Tang, X., Zhang, J., Pang, Z., Hu, S., Tian, J., & Bao, S. (2017). The eastern Tibetan Plateau geothermal belt, western China: Geology, geophysics, genesis, and hydrothermal system. *Tectonophysics*, *717*, 433–448. https://doi.org/10.1016/j.tecto.2017.08.035

Tapponnier, P., Peltzer, G., Le Darin, A. Y., & Armijo, R. (1982). Propagating extrusion tectonics in Asia: New insights from simple experiments with plasticine. *Geology*, *10*, 611–616. https://doi.org/10.1130/0091-7613(1982)10%3C611:PETIAN%3E2.0.CO;2

Tapponnier, P., Zhiqin, X., Roger, F., Meyer, B., Arnaud, N., Wittlinger, G., & Jingsui, Y. (2001). Oblique stepwise rise and growth of the Tibetan Plateau. *Science*, *294*, 1671–1677. https://doi.org/10.1126/science.105978

Tong, Y., Yang, Z., Gao, L., Wang, H., Zhang, X.-D., An, C.-Z., et al. (2015). Paleomagnetism of Upper Cretaceous red-beds from the eastern Qiangtang Block: Clockwise rotations and latitudinal translation during the India-Asia collision. *Journal of Asian Earth Sciences*, *114*, 732–749. https://doi.org/10.1016/j.jseaes.2015.08.016

Tong, Y., Yang, Z., Mao, C., Pei, J., Pu, Z., & Xu, Y. (2017). Paleomagnetism of Eocene red-beds in the eastern part of the Qiangtang Terrane and its implications for uplift and southward crustal extrusion in the southeastern edge of the Tibetan Plateau. *Earth and Planetary Science Letters*, *475*, 1–14. https://doi.org/10.1016/j.epsl.2017.07.026

Wang, E., & Burchfield, B. C. (2000). Late Cenozoic to Holocene deformation in southwestern Sichuan and adjacent Yunnan, China, and its role in formation of the southeastern part of the Tibetan Plateau. *Geological Society of America Bulletin*, *112*(3), 413–423. https://doi.org/10.1130/0016-7606(2000)112%3C413:LCTHDI%3E2.0.CO;2

Wang, X., Zhang, J., Jiang, W., & Wang, D. (2019). Gravity field and deep seismogenic environment in the Longmen Shan and adjacent regions, Eastern Tibetan Plateau. *Journal of Asian Earth Sciences*, *176*, 79–87. https://doi.org/10.1016/j.jseaes.2019.02.003

Weil, A. B., & Yonkee, A. (2009). Anisotropy of magnetic susceptibility in weakly deformed red beds from the Wyoming salient, Sevier thrust belt: Relations to layer-parallel shortening and orogenic curvature. *Lithosphere*, *1*(4), 235–256. https://doi.org/10.1130/L42.1

Wu, T., Xiao, L., Wilde, S. A., Ma, C.-Q., & Zhou, J.-X. (2017). A mixed source for the Late Triassic Garze-Daocheng granitic belt and its implications for the tectonic evolution of the Yidun arc belt, eastern Tibetan Plateau. *Lithos*, *288-289*, 214–230. https://doi.org/10.1016/j.lithos.2017.07.002

Zhang, Y., Huang, W., Huang, B., van Hinsbergen, D. J. J., Yang, T., Dupont-Nivet, G., & Guo, Z. (2018). 53–43 Ma deformation of eastern Tibet revealed by three stages of tectonic rotation in the Gongjue basin. *Journal of Geophysical Research: Solid Earth*, *123*, 3320–3338. https://doi.org/10.1002/2018JB015443

Zhang, Y.-Z., Replumaz, A., Wang, G.-C., Leloup, P. H., Gautheron, C., Bernet, M., et al. (2015). Timing and rate exhumation along the Litang fault system, implication for fault reorganization in Southeast Tibet. *Tectonics*, *34*, 1219–1243. https://doi.org/10.1002/2014TC003671

Zijderveld, J. D. (1967). A. C. demagnetization of rocks: Analysis of results. In D. W. Collinson, K. M. Creer, & S. K. Runcorn (Eds.), *Methods in paleomagnetism, developments in Solid Earth Geophysics* (Vol. 3, pp. 254–286). New York: Elsevier. https://doi.org/10.1016/B978-1-4832-2894-5.50049-5